

# Large Inverse Tunnel Magnetoresistance in Magnetic Tunnel Junctions with an $\text{Fe}_3\text{O}_4$ Electrode

Shoma Yasui,<sup>1</sup> Syuta Honda<sup>2</sup>, Jun Okabayashi,<sup>3</sup> Takashi Yanase,<sup>4</sup>  
Toshihiro Shimada,<sup>4</sup> and Taro Nagahama<sup>1,\*</sup>

<sup>1</sup>Graduate School of Chemical Sciences and Engineering, Hokkaido University, Sapporo, Hokkaido 060-8628, Japan

<sup>2</sup>Pure and Applied Physics, Kansai University, Suita, Osaka 564-8680, Japan

<sup>3</sup>Research Center for Spectrochemistry, The University of Tokyo, Bunkyo-ku, Tokyo 113-0033, Japan

<sup>4</sup>Graduate School of Engineering, Hokkaido University, Sapporo, Hokkaido 060-8628, Japan



(Received 4 November 2020; revised 31 January 2021; accepted 5 February 2021; published 15 March 2021)

Spinel-type magnetite  $\text{Fe}_3\text{O}_4$  is predicted to be a half-metal material with negative spin polarization. However, magnetic tunnel junctions (MTJs) using an  $\text{Fe}_3\text{O}_4$  electrode exhibit a small tunnel magnetoresistance (TMR) effect, the sign of which has not been established experimentally. The development of  $\text{Fe}_3\text{O}_4$  as an excellent TMR material requires a better understanding of the characteristics of the interface and the phase transition of  $\text{Fe}_3\text{O}_4$  called the Verwey transition. We fabricate MTJs using epitaxial  $\text{Fe}_3\text{O}_4$ -based stacks on  $\text{MgO}(001)$  substrates and find a large inverse TMR ratio of  $-55.8\%$  at 80 K, which corresponds to 126% by the optimistic definition of the TMR ratio. The temperature dependence of the TMR ratio is significantly affected by the Verwey transition. Moreover, we investigate the dependence of TMR on oxygen partial pressure during  $\text{Fe}_3\text{O}_4$  deposition. It is found that the magneto-transport properties of the MTJs show different behaviors depending on the oxygen partial pressure because the Verwey transition is sensitive to the oxygen concentration. Furthermore, the electronic and magnetic properties at the interfacial regions are investigated by x-ray magnetic spectroscopy and first-principles calculation. These findings greatly support the use of  $\text{Fe}_3\text{O}_4$  in spintronic devices and should lead to further developments in oxide spintronics.

DOI: 10.1103/PhysRevApplied.15.034042

## I. INTRODUCTION

Since magnetite  $\text{Fe}_3\text{O}_4$  exhibits ferrimagnetic and conductive properties at room temperature, numerical studies have been conducted using  $\text{Fe}_3\text{O}_4$  as a spintronic material [1–3]. In particular, it was predicted theoretically to have electronic states corresponding to a half-metal with perfect negative polarization of  $-100\%$  at the Fermi level [4,5], thereby creating a large tunnel magnetoresistance (TMR) effect, which is a key technology in spintronics [6]. Therefore, many researchers have worked to create large TMR in magnetic tunnel junctions (MTJs) employing  $\text{Fe}_3\text{O}_4$ . However, this has not yet been successful because of the difficulty of forming an abrupt interface between the  $\text{Fe}_3\text{O}_4$  and insulating barriers [2,7–14]. Moreover, even the sign of the TMR depends on the growth conditions. The reasons behind these unexpected tunneling characteristics have not been clarified, and it remains an open question as to whether  $\text{Fe}_3\text{O}_4$  acts as a high-functional material in MTJs.

The half-metallicity of  $\text{Fe}_3\text{O}_4$  has been investigated theoretically and experimentally. Yanase and Shiratori pointed out that only majority spin electrons have a gap at the Fermi level in  $\text{Fe}_3\text{O}_4$  [4], and many theoretical studies involving *ab initio* calculations have confirmed this [5,15,16]. The spin polarization of  $\text{Fe}_3\text{O}_4$  was estimated by spectroscopic experiments to be  $-80\%$  and  $-60\%$  for the (111) and (100) surfaces, respectively [15,17–19]. These results clearly indicate that  $\text{Fe}_3\text{O}_4$  has a high spin polarization. In contrast, the TMR ratio in  $\text{Fe}_3\text{O}_4$  MTJs has remained low. Suzuki *et al.* investigated a number of  $\text{Fe}_3\text{O}_4$  MTJs using an  $\text{La}_{1-x}\text{Sr}_x\text{MnO}_3$  electrode [20–25] and observed a TMR of  $-33\%$  in a high magnetic field of 7 T [25]. Kado observed variation in the TMR ratio from  $-28\%$  to  $+30\%$  and found a correlation between the sign of the TMR and the junction resistance in  $\text{Fe}_3\text{O}_4/\text{MgO}$  [7]. Marnitz *et al.* argued that Mg migration from a  $\text{MgO}$  barrier could change the sign of TMR [8]. In a previous study, we obtained an inverse TMR effect of  $-15\%$  in a MTJ using  $\text{Fe}_3\text{O}_4(110)$  electrodes [14], and also observed phenomena like the inverse tunnel magnetocapacitance effect [26].

\*nagahama@eng.hokudai.ac.jp

The important factors for enhancing the TMR effect are as follows: (1) utilizing a counter electrode with high spin polarization and (2) optimizing the crystallinity at the  $\text{Fe}_3\text{O}_4$ /barrier interface. In this paper, we fabricate fully epitaxial MTJs of  $\text{Fe}_3\text{O}_4(001)/\text{MgO}(001)/\text{Fe}(001)$  and succeed in observing a large inverse TMR effect of  $-55.8\%$  at 80 K, which exceeds 100% when we adopt an optimistic definition of the inverse TMR ratio. We find that the TMR ratio strongly depends on the partial oxygen pressure during the  $\text{Fe}_3\text{O}_4$  deposition. Furthermore, in order to clarify the microscopic mechanism, we employ element-specific x-ray magnetic spectroscopy and band-structure calculations. We discuss the relation between TMR and electronic structures.

## II. EXPERIMENTS

Multilayers are prepared by molecular beam epitaxy in a chamber at a base pressure of  $10^{-8}$  Pa. The layer structure of the MTJs is  $\text{MgO}(100)/\text{buffer}-\text{MgO}(20 \text{ nm})/\text{NiO}(5 \text{ nm})/\text{Fe}_3\text{O}_4(60 \text{ nm})/\text{MgO}(2.5 \text{ nm})/\text{Fe}(10 \text{ nm})/\text{Au}(30 \text{ nm})$ . The 20-nm MgO buffer layer is grown at a substrate temperature ( $T_{\text{sub}}$ ) of 673 K on the  $\text{MgO}(100)$  substrate that is prebaked at 1073 K. The NiO layer is deposited at 573 K to prevent the diffusion of Mg from the buffer layer and substrate. The  $\text{Fe}_3\text{O}_4$  layer is grown by reactive deposition at  $T_{\text{sub}}$  of 573 K under an  $\text{O}_2$  atmosphere. We prepare  $\text{Fe}_3\text{O}_4$  layers at different oxygen partial pressures of  $4 \times 10^{-4}$ ,  $1 \times 10^{-4}$ , and  $5 \times 10^{-5}$  Pa for Samples 1, 2, and 3, respectively. The  $\text{Fe}_3\text{O}_4$  layers are then annealed at 873 K for 30 min in an  $\text{O}_2$  atmosphere at  $1 \times 10^{-4}$  Pa. The MgO barrier layer is formed by evaporation of single-crystal MgO at room temperature followed by annealing at 423 K for 30 min. The 10-nm-thick Fe layer and Au cap layer are deposited at room temperature.

The crystallinity and epitaxial growth of the films are monitored by reflection high-energy electron diffraction (RHEED) and x-ray diffraction (XRD). After the growth of the multilayered stacks, MTJ structures with a junction area of  $10 \times 10 \mu\text{m}^2$  are patterned by a conventional microfabrication process with photolithography and Ar ion milling. The current-voltage ( $I-V$ ) characteristics and magnetoresistance are measured by the dc four-probe method. X-ray absorption spectroscopy (XAS) and x-ray magnetic circular dichroism (XMCD) are performed at BL-7A in Photon Factory at the High Energy Accelerator Research Organization (KEK). A magnetic field of  $\pm 1$  T is applied along the incident polarized soft-x-ray beams, with the circularly polarized absorption signals defined as  $\mu^+$  and  $\mu^-$ . The XAS and XMCD are defined by  $(\mu^+ + \mu^-)/2$  and  $\mu^+ - \mu^-$ , respectively. The total electron yield mode is adopted. All XAS and XMCD measurements are carried out at room temperature.

## III. RESULTS AND DISCUSSION

The epitaxial growth and crystal structure are confirmed by XRD and RHEED. The lattice constants in bulk are 4.21 Å for MgO ( $a_{\text{MgO}}$ ), 8.396 Å for  $\text{Fe}_3\text{O}_4$  ( $a_{\text{Fe}_3\text{O}_4}$ ), and 2.87 Å for Fe ( $a_{\text{Fe}}$ ) (4.073 Å for  $\sqrt{2}a_{\text{Fe}}$ ). A clear streak RHEED pattern is observed for the  $\text{Fe}_3\text{O}_4$  layer as shown in Fig. 1(a), indicating the formation of a film with a flat surface. Furthermore, a characteristic  $\sqrt{2} \times \sqrt{2}$  R45 superlattice peak is also observed on the  $\text{Fe}_3\text{O}_4(001)$  surface [27]. The surfaces of MgO also show a clear streak pattern as shown in Fig. 1(b). This confirms that the MTJ consists of layer-by-layer epitaxial growth. For Fig. 1(c), the RHEED pattern is slightly spotty, meaning epitaxial growth with a roughness of 2 nm in the surface [an Atomic Force Microscope (AFM) image of Fe surface is shown in Fig. S1 in the Supplemental Material [28]]. We also perform TEM observation to obtain a cross-section image of MTJs and then atomically flat interfaces are confirmed (see Fig. S2 in the Supplemental Material [28]).

In the XRD profile for the  $\text{Fe}_3\text{O}_4/\text{MgO}/\text{Fe}$  film in Fig. 1(d), only the (004) and (008) peaks are found for  $\text{Fe}_3\text{O}_4$ , which is consistent with the RHEED results. The XRD peaks of  $\text{Fe}_3\text{O}_4(004)$  and  $\text{MgO}(002)$  are nearly the same at  $42.98^\circ$  and  $43.30^\circ$ , respectively. The lattice constant for the  $c$  axis of  $\text{Fe}_3\text{O}_4$  is 8.369 Å, which corresponds to a difference of 0.32% from the bulk value of 8.396 Å. This results in a very small lattice mismatch with MgO of 0.29%. The  $\text{Fe}(002)$  peak is also observed because of epitaxial growth of the upper electrode.

The TMR effect of Sample 1 deposited at  $4 \times 10^{-4}$  Pa is shown in Fig. 2(a). The TMR is  $-9.6\%$  at room temperature and  $-55.8\%$  at 80 K. The obtained inverse TMR indicates that the polarization of  $\text{Fe}_3\text{O}_4$  ( $P_{\text{Fe}_3\text{O}_4/\text{MgO}}$ ) is negative, which is consistent with the band calculations.

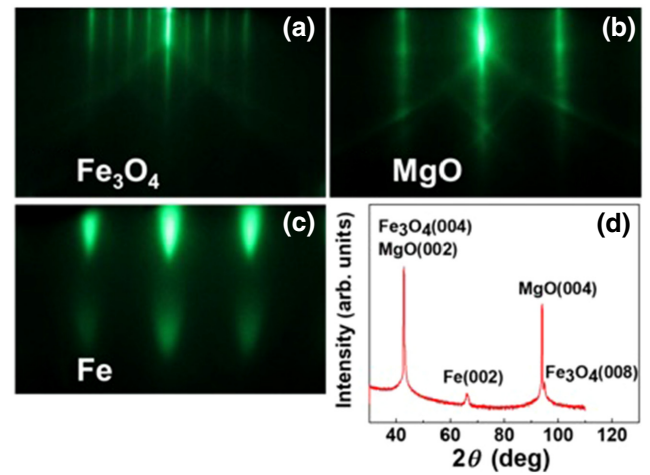


FIG. 1. RHEED patterns for each layer: (a)  $\text{Fe}_3\text{O}_4$ , (b) MgO, and (c) Fe. (d) XRD profile for  $\text{MgO}(001)/\text{Fe}_3\text{O}_4(001)/\text{MgO}(001)/\text{Fe}(001)$ .

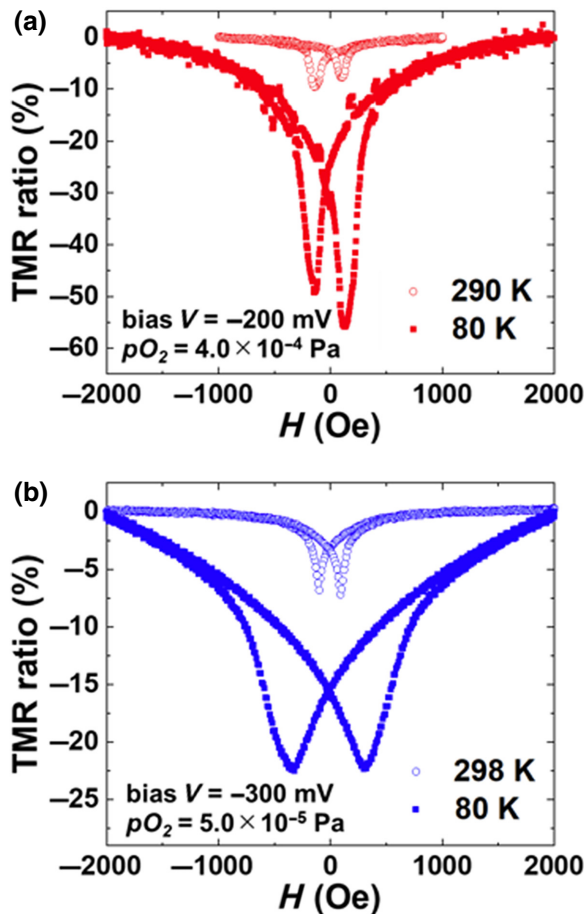


FIG. 2. TMR curves for  $\text{Fe}_3\text{O}_4(001)/\text{MgO}(001)/\text{Fe}(001)$  MTJs deposited in an oxygen atmosphere at (a)  $4 \times 10^{-4}$  Pa (Sample 1) and (b)  $5 \times 10^{-5}$  Pa (Sample 3). The TMR curves are measured at room temperature and 80 K.

With respect to the spin polarization, the polarization at 80 K is estimated to be  $P_{\text{Fe}_3\text{O}_4/\text{MgO}} = -0.55$  under the assumption that the polarization of  $\text{MgO}/\text{Fe}$  ( $P_{\text{Fe}/\text{MgO}}$ ) is 0.7 based on the TMR ratio of  $\text{Fe}/\text{MgO}/\text{Fe}$  at 9 K [29]. At room temperature,  $P_{\text{Fe}_3\text{O}_4/\text{MgO}}$  is estimated to be 0.09, under the assumption that  $P_{\text{Fe}/\text{MgO}} = 0.56$  at 300 K based on Ref. [30].  $P_{\text{Fe}_3\text{O}_4}$  may be underestimated because  $P_{\text{Fe}/\text{MgO}}$  in  $\text{Fe}_3\text{O}_4/\text{MgO}/\text{Fe}$  may be smaller than that in  $\text{Fe}/\text{MgO}/\text{Fe}$  because annealing is not performed after deposition of the upper electrode. Although the TMR ratios differ between room temperature and 80 K, the magnetic fields of the maximum TMR, which are associated with magnetic characteristics, are very similar, as shown in Fig. 2(a).

Note that the TMR ratio of  $-55.8\%$  is derived by the conventional definition of

$$\text{TMR}(\%) = \frac{(R_{\text{AP}} - R_{\text{P}})}{R_{\text{P}}} \times 100, \quad (1)$$

where  $R_{\text{P}}$  and  $R_{\text{AP}}$  are the tunnel resistance for parallel and antiparallel magnetic configurations, respectively. In conventional MTJs, such as  $\text{Fe}/\text{MgO}/\text{Fe}$ , definition (1) is called the “optimistic definition” because the maximum TMR ratio reaches infinity. However, in the case of inverse TMR observed in  $\text{Fe}_3\text{O}_4/\text{MgO}/\text{Fe}$ , the maximum value is limited to 100% by this definition. There is another definition as follows:

$$\text{TMR}(\%) = \frac{(R_{\text{AP}} - R_{\text{P}})}{R_{\text{AP}}} \times 100, \quad (2)$$

which is called the pessimistic definition for conventional MTJs because the maximum ratio is 100%, although it is an “optimistic” definition for inverse TMR. Note that the inverse TMR of  $-55.8\%$  calculated by definition (1) corresponds to  $-126\%$  by definition (2). The shape of the TMR curve is sharp at its maximum, which indicates a reduced antiparallel state, meaning that there is still some room for improvement in the TMR ratio.

The TMR curves for Sample 3 are shown in Fig. 2(b). At 80 K, the TMR ratio is only  $-22.5\%$ , which is smaller than that for Sample 1. In addition, the shape of the TMR curve broadens to higher magnetic fields at low temperatures, implying that the magnetic characteristics vary. The change of the magnetic property of Sample 3 is also confirmed by comparison of magnetic hysteresis between high and low temperature, as shown in Fig. S3 of the Supplemental Material [28]. At low temperature,  $\text{Fe}_3\text{O}_4/\text{MgO}/\text{Fe}$  multilayer shows a clear two-step hysteresis loop with large coercive field, although the hysteresis is narrow at high temperature because of close coercive field between  $\text{Fe}_3\text{O}_4$  and Fe, like Sample 1.

The shapes of TMR curves are not square, which is different from that in a conventional MTJ like  $\text{Co-Fe-B}/\text{MgO}/\text{Co-Fe-B}$ . This could be attributed to the moderate magnetic reversal of  $\text{Fe}_3\text{O}_4$  and aforementioned close coercive field between  $\text{Fe}_3\text{O}_4$  and Fe. The anisotropic magnetoresistance (AMR) of  $\text{Fe}_3\text{O}_4$  can be included in the background of the TMR curves. However, it should be a small effect because the AMR of  $\text{Fe}_3\text{O}_4$  is much smaller than the TMR and the sign of the effect is opposite (see Fig. S4 in the Supplemental Material [28]).

To understand the difference between Samples 1 and 3, we investigate the temperature dependence of TMR ratio for the three samples, as shown in Fig. 3(a). At room temperature, all the TMR ratios are about  $-10\%$ , and the absolute values then increase with decreasing temperature. For Sample 1, the TMR ratio increases monotonically as the temperature decreases to 80 K, whereas the TMR for Samples 2 and 3 exhibits a maximum at 125 K. At all temperatures, the TMR ratio of Sample 3 is larger than that of Sample 2. The TMR ratios strongly depend on the  $\text{O}_2$  atmosphere during the formation of  $\text{Fe}_3\text{O}_4$ , and

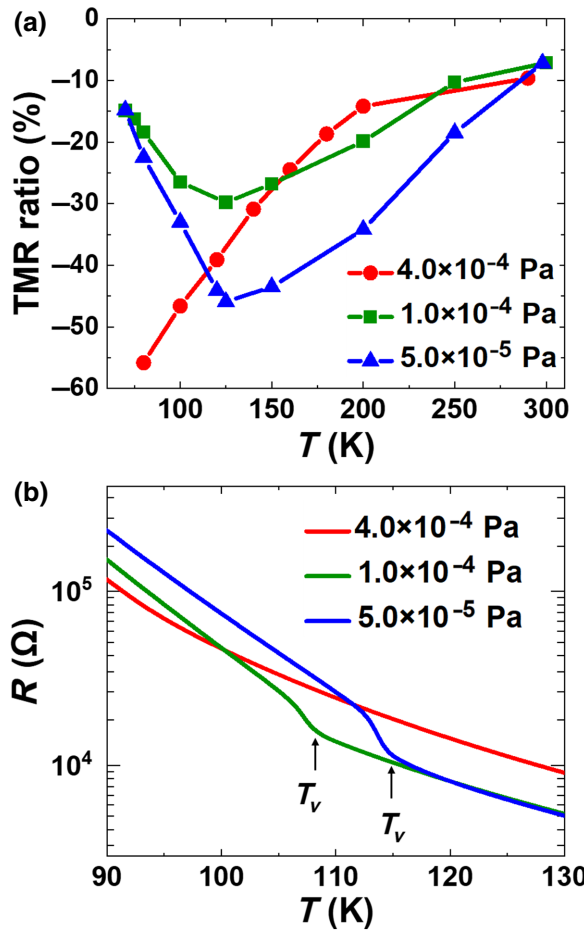


FIG. 3. (a) Temperature dependence of TMR ratio of the MTJs. The resistance at 2000 Oe is employed as  $R_p$ . (b) Resistance of  $\text{Fe}_3\text{O}_4$  electrodes deposited in various oxygen atmospheres.

exhibit a maximum at the Verwey temperature, which is a well-known phase transition in  $\text{Fe}_3\text{O}_4$  [30–32].

To confirm the Verwey temperature of each MTJ, we measure the temperature dependence of the resistance of  $\text{Fe}_3\text{O}_4$  electrodes, as shown in Fig. 3(b). All the  $\text{Fe}_3\text{O}_4$  electrodes exhibit an exponential increase in resistance, and Samples 2 and 3 exhibit an abrupt increase in resistance at 108 and 114 K, respectively. In contrast, Sample 1 exhibits no significant change in resistivity from 300 to 80 K, the same as the TMR ratio. This result strongly supports that the Verwey transition is responsible for the temperature dependence of TMR shown in Fig. 3(a). Note that Sample 3, for which the TMR ratio is larger than Sample 2, has a higher Verwey temperature that is closer to that of the bulk material.

For Sample 1, there remains a possibility that the  $\text{Fe}_3\text{O}_4$  is overoxidized, resulting in the presence of the  $\gamma\text{-Fe}_2\text{O}_3$  phase. Since both  $\text{Fe}_3\text{O}_4$  and  $\gamma\text{-Fe}_2\text{O}_3$  form a spinel structure and the lattice constants are almost the same, it is difficult to distinguish them using XRD [33]. Thus, as

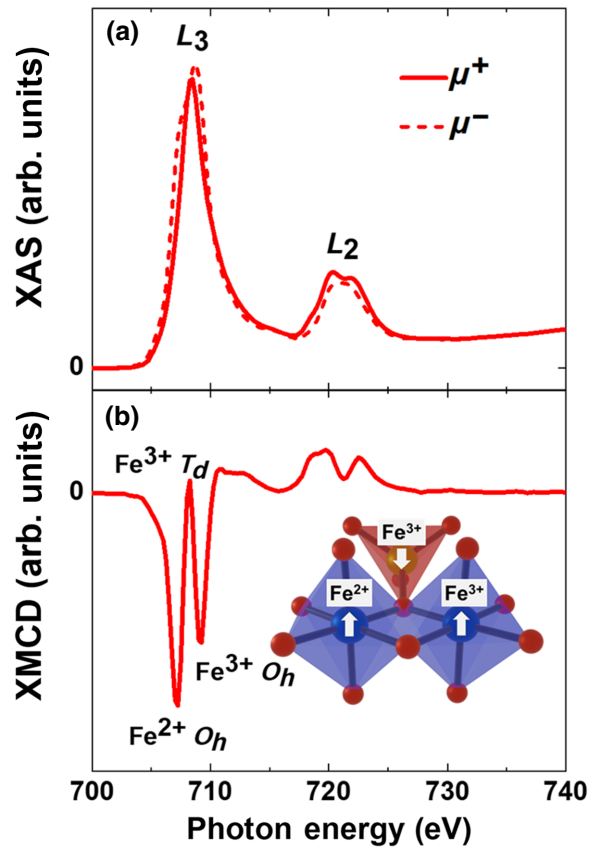


FIG. 4. (a) XAS and (b) XMCD of 50-nm-thick  $\text{Fe}_3\text{O}_4$  films prepared under oxygen pressure of  $4 \times 10^{-4}$  Pa (Sample 1). Inset shows an illustration for A (red) and B (blue) sites.

shown in Fig. 4, we conduct XAS and XMCD of 50-nm-thick  $\text{Fe}_3\text{O}_4(001)$  films prepared using an oxygen partial pressure of  $4 \times 10^{-4}$  Pa with a 1-nm-thick MgO capping layer. The complex differential spectral line shape in the  $L_3$  and  $L_2$  edge XMCD corresponds to the overlapping of three kinds of Fe site multiplet structures with antiparallel coupling. The XMCD line shape indicates the formation of a spinel-type structure because the spin-down states of  $\text{Fe}^{2+}$  and  $\text{Fe}^{3+}$  in  $O_h$  symmetry (B site) with spin-up states of  $\text{Fe}^{3+}$  ( $T_d$ : A site) can be clearly seen as antiparallel coupling. The intensity of the  $\text{Fe}^{2+}$  component can be monitored by the degree of oxidation. Within the probing depth of XAS and XMCD of 3 nm from the sample surface, the interfacial regions are detected, including the capping MgO layer. The intensities of  $\text{Fe}^{2+}$  and  $\text{Fe}^{3+}$  in  $O_h$  are almost similar to those of previous studies of XMCD in  $\text{Fe}_3\text{O}_4$  [34–37], meaning that the  $\text{Fe}_3\text{O}_4$  with stoichiometric B site is synthesized, but the Verwey transition is absent in Sample 1. Since the Verwey transition has been reported to be very sensitive to oxygen composition [38,39], the  $\text{O}_2$  partial pressure significantly influences the transport of  $\text{Fe}_3\text{O}_4$ . Compared with previous reports [37,40], the ratio

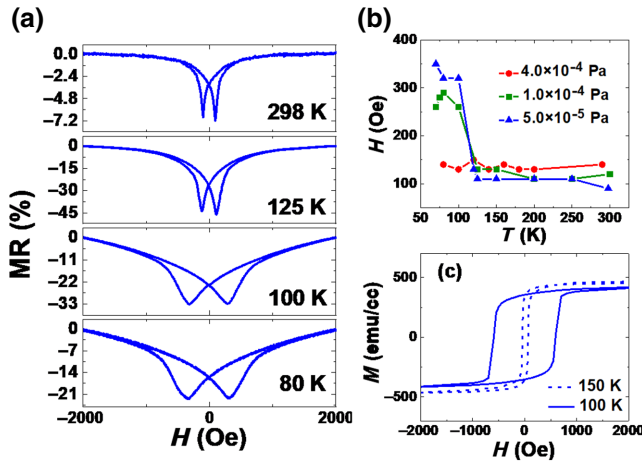


FIG. 5. (a) TMR curves for  $\text{Fe}_3\text{O}_4(001)/\text{MgO}(001)/\text{Fe}(001)$  deposited at  $5 \times 10^{-5}$  Pa at various temperatures. (b) Temperature dependence of the magnetic field where the TMR ratio exhibits maximum values. (c) Magnetic hysteresis curves of an  $\text{Fe}_3\text{O}_4(001)$  film deposited at  $5 \times 10^{-5}$  Pa above and below the Verwey temperature.

of  $\text{Fe}^{3+}(T_d)$  component decreased, meaning less occupation of A sites. At the moment, it is not conclusively known whether A site vacancies contribute to the large TMR ratio because  $\text{Fe}^{3+}$  in A site provides no conduction electrons. Further investigations are required to clarify the role of the A site in  $\text{Fe}_3\text{O}_4$  for TMR.

The shape of the TMR curves also provides clues for understanding TMR. In Fig. 5(a), the TMR curves of Sample 3 are shown in terms of temperature. From 298 to 125 K, the tunnel resistance exhibits peaks at  $\pm 100$  Oe, whereas at temperatures under 100 K, the coercive field for TMR suddenly increases to  $\pm 320$  Oe. The switching magnetic fields are plotted in Fig. 5(b) as functions of temperature. It is apparent that the Verwey transition enhances the coercive magnetic fields of  $\text{Fe}_3\text{O}_4$  below the Verwey temperature [41,42]. The change in coercive force of  $\text{Fe}_3\text{O}_4$  films is also confirmed by superconducting quantum interference device measurements of  $\text{MgO}(100)/\text{Fe}_3\text{O}_4(50\text{ nm})$  film, as shown in Fig. 5(c).

Since we use a MgO/Fe counter electrode, the tunneling process, namely coherent or diffusive tunneling, needs to be discussed. In Fe/MgO/Fe MTJs, since coherent tunneling through the  $\Delta_1$  band dominates the transport, a large TMR is observed. The  $\Delta_1$  band consists of  $s$ ,  $p_z$ , and  $d_{3z^2-r^2}$ . In addition, if we consider a simple picture of the transport in  $\text{Fe}_3\text{O}_4$ , the main contributions to the transport are the  $t_{2g}$  states, which consist of  $d_{xy}$ ,  $d_{yz}$ , and  $d_{zx}$  orbital symmetries. Since the wave functions of the  $t_{2g}$  state of  $\text{Fe}_3\text{O}_4$  and the  $\Delta_1$  band of Fe are not hybridized, the tunneling process via the  $t_{2g}$  state may be diffusive tunneling in the  $\text{Fe}_3\text{O}_4/\text{MgO}/\text{Fe}(001)$  junction. To see the coherent tunneling in  $\text{Fe}_3\text{O}_4/\text{MgO}/\text{Fe}$  in detail, we calculate

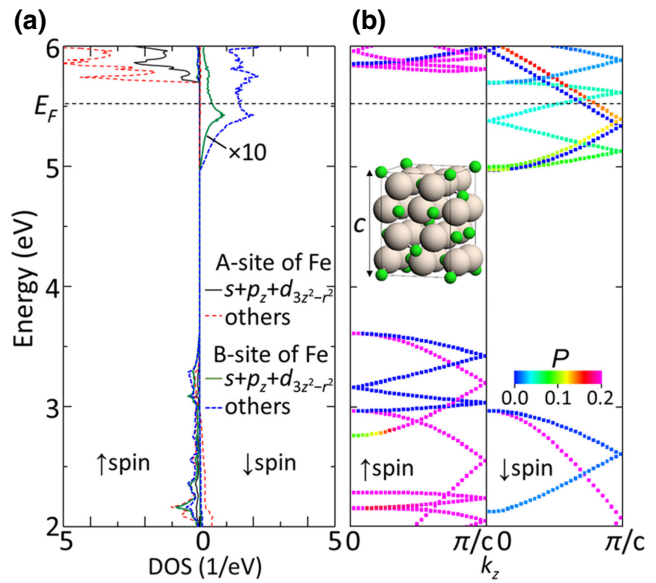


FIG. 6. Calculation results of (a) spin-dependent local density of states (DOS) and (b)  $E$ - $k$  dispersion relation between  $\mathbf{k} = (0, 0, 0)$  and  $\mathbf{k} = (0, 0, \pi/c)$ . The unit cell for  $E$ - $k$  calculations is shown in (b). In (a), the DOS of the sum of the  $s$ ,  $p_z$ , and  $d_{3z^2-r^2}$  orbitals (the coherent orbitals) of the B site of Fe ions in the conduction band is shown magnified 10 times. The percentages of the summation of the coherent orbitals ( $P$ ), which are hybridized with the wave functions transmitted through MgO in an  $\text{Fe}_3\text{O}_4/\text{MgO}/\text{Fe}$  junction, are plotted in color.

the electronic structure for an optimized  $\text{Fe}_3\text{O}_4$  supercell structure, as shown in Fig. 6(b). We call the  $s$ ,  $p_z$ , and  $d_{3z^2-r^2}$  orbitals of  $\text{Fe}_3\text{O}_4$  the coherent orbitals, and other orbitals the diffusive orbitals. The first-principles calculation is performed using the VASP code with the PAW potentials [43] in the generalized gradient approximation with Perdew-Burke-Ernzerhof functional [44,45]. A correction of the Coulomb interaction  $U$  of 4.5 eV is assumed for the Fe ions [46,47]. The cutoff energy is set to 400 eV and the crystal momentum  $k$  sampling mesh is set to  $(k_x, k_y, k_z) = 21, 21, 21$ .

Figure 6(a) shows the density of states for spin-up and spin-down states. Since the spin-down states cross the Fermi level ( $E_F$ ), half-metallicity is reproduced. At  $E_F$ , the diffusive orbitals of the B site of the Fe ion with spin down (thick blue dotted curve) mainly cross the small contribution of the coherent orbitals (thick green solid curve). Figure 6(b) shows the energy-momentum ( $E$ - $k$ ) dispersion relation along  $(k_x, k_y, k_z) = (0, 0, 0) - (0, 0, \pi/c)$  in the Brillouin zone. The color of the plot indicates the percentage of the sum of the coherent orbitals, which hybridize with the  $\Delta_1$  band at the interface with the Fe electrode layer. The bands near  $E_F$  contain about 10% of the coherent orbitals. Therefore, the coherent tunneling can take place with these bands in  $\text{Fe}_3\text{O}_4$ . Another possibility is diffusive transport via scattering at the  $\text{Fe}_3\text{O}_4/\text{MgO}$  interface

due to the symmetry mismatch of the wave functions. The half-metallicity of  $\text{Fe}_3\text{O}_4$  can bring about large TMR even though the tunneling is not coherent.

Important clues for distinguishing between coherent and diffusive tunneling can be found by comparing a MTJ with a MgO barrier and an amorphous  $\text{Al}_2\text{O}_3$  barrier. Further development of the fabrication techniques for MTJs using  $\text{Fe}_3\text{O}_4$  is necessary in order to investigate the tunneling process experimentally.

#### IV. CONCLUSION

In conclusion, we fabricate MTJs of  $\text{Fe}_3\text{O}_4(001)/\text{MgO}(001)/\text{Fe}(001)$ , the quality of which is confirmed by XRD and XMCD. The MTJs exhibit a large inverse TMR effect of  $-55.8\%$ , which is comparable with the theoretical prediction. If we use an optimistic definition for the inverse TMR, the TMR ratio achieves  $126\%$ , which is the largest value for  $\text{Fe}_3\text{O}_4$  MTJs. We find that the TMR ratio strongly depends on the deposition conditions of the  $\text{Fe}_3\text{O}_4$  layer, which may be attributable to the Verwey transition in  $\text{Fe}_3\text{O}_4$ . The possibility of coherent tunneling is discussed on the basis of *ab initio* calculations through the  $s$ ,  $p_z$ , and  $d_{3z^2-r^2}$  orbitals in  $\text{Fe}_3\text{O}_4$  at the Fermi level, which are hybridized with the  $\Delta_1$  band of Fe via the MgO tunnel barrier. These results obtained in this study could pave the way for the development of high-functional fully oxide spintronic devices.

#### ACKNOWLEDGMENTS

We would like to express our gratitude to Professor Uemura's group and Professor Tokeshi's group at Hokkaido University for their cooperation in the microfabrication. This work is partly supported by JSPS KAKENHI Grants No. 15H05702, No. 18H01465, and No. 18H01485, the Collaborative Research Program of the Institute for Chemical Research, Kyoto University (Grant No. 2015-74), the Center for Spintronics Research Network (Grant No. 2019-21), and the Open Facility, Hokkaido University Souse Hall and Nanotechnology Collaborative Research of Hokkaido University. Parts of the synchrotron radiation experiments were performed under the approval of the Photon Factory Program Advisory Committee, KEK (No. 2019G121).

materials based on oxide thin films and artificial heteroepitaxial multilayers, *Physica Status Solidi A* **208**, 232 (2011).

- [3] M. Bibes and A. Barthelemy, Oxide spintronics, *IEEE Trans. Electron Devices* **54**, 1003 (2007).
- [4] A. Yanase and K. Siratori, Band structure in the high temperature phase of  $\text{Fe}_3\text{O}_4$ , *J. Phys. Soc. Jpn* **53**, 312 (1984).
- [5] Z. Zhang and S. Satpathy, Electron states, magnetism, and the verwey transition in magnetite, *Phys. Rev. B Condens. Matter* **44**, 13319 (1991).
- [6] M. Julliere, Tunneling between ferromagnetic films, *Phys. Lett. A* **54**, 225 (1975).
- [7] T. Kado, Large room-temperature inverse magnetoresistance in tunnel junctions with a  $\text{Fe}_3\text{O}_4$  electrode, *Appl. Phys. Lett.* **92**, 092502 (2008).
- [8] L. Marnitz, K. Rott, S. Niehörster, C. Klewe, D. Meier, S. Fabretti, M. Witzik, A. Krampf, O. Kuschel, T. Schemme, K. Kuepper, J. Wollschläger, A. Thomas, G. Reiss, and T. Kuschel, Sign change in the tunnel magnetoresistance of  $\text{Fe}_3\text{O}_4/\text{MgO}/\text{Co-Fe-B}$  magnetic tunnel junctions depending on the annealing temperature and the interface treatment, *AIP Adv.* **5**, 047103 (2015).
- [9] D. Reisinger, P. Majewski, M. Opel, L. Alff, and R. Gross, *Room Temperature Tunneling Magnetoresistance in Magnetite Based Junctions: Influence of Tunneling Barrier*. <http://arxiv.org/abs/cond-mat/0407725>
- [10] F. Greullet, E. Snoeck, C. Tiusan, M. Hehn, D. Lacour, O. Lenoble, C. Magen, and L. Calmels, Large inverse magnetoresistance in fully epitaxial  $\text{Fe}/\text{Fe}_3\text{O}_4/\text{MgO}/\text{Co}$  magnetic tunnel junctions, *Appl. Phys. Lett.* **92**, 053508 (2008).
- [11] H. Matsuda, M. Takeuchi, H. Adachi, M. Hiramoto, N. Matsukawa, A. Odagawa, K. Setsune, and H. Sakakima, Fabrication and magnetoresistance properties of spin-dependent tunnel junctions using an epitaxial  $\text{Fe}_3\text{O}_4$  film, *Jpn. J. Appl. Phys.* **41**, L387 (2002).
- [12] K. S. Yoon, J. H. Koo, Y. H. Do, K. W. Kim, C. O. Kim, and J. P. Hong, Performance of  $\text{Fe}_3\text{O}_4/\text{AlO}_x/\text{CoFe}$  magnetic tunnel junctions based on half-metallic  $\text{Fe}_3\text{O}_4$  electrodes, *J. Magn. Magn. Mater.* **285**, 125 (2005).
- [13] A. M. Bataille, R. Mattana, P. Seneor, A. Tagliaferri, S. Gota, K. Bouzehouane, C. Deranlot, M.-J. Guittet, J.-B. Moussy, C. de Nadaï, N. B. Brookes, F. Petroff, and M. Gautier-Soyer, On the spin polarization at the  $\text{Fe}_3\text{O}_4/\gamma\text{-Al}_2\text{O}_3$  interface probed by spin-resolved photoemission and spin-dependent tunneling, *J. Magn. Magn. Mater.* **316**, e963 (2007).
- [14] T. Nagahama, Y. Matsuda, K. Tate, T. Kawai, N. Takahashi, S. Hiratani, Y. Watanabe, T. Yanase, and T. Shimada, Magnetic properties of epitaxial  $\text{Fe}_3\text{O}_4$  films with various crystal orientations and tunnel magnetoresistance effect at room temperature, *Appl. Phys. Lett.* **105**, 102410 (2014).
- [15] W. Wang, J.-M. Mariot, M. C. Richter, O. Heckmann, W. Ndiaye, P. De Padova, A. Taleb-Ibrahimi, P. Le Fèvre, F. Bertran, F. Bondino, E. Magnano, J. Krempaský, P. Blaha, C. Cacho, F. Parmigiani, and K. Hricovini,  $\text{Fe t}_{2g}$  band dispersion and spin polarization in thin films of  $\text{Fe}_3\text{O}_4(001)/\text{MgO}(001)$ : Half-metallicity of magnetite revisited, *Phys. Rev. B Condens. Matter* **87**, 085118 (2013).

[1] J.-B. Moussy, From epitaxial growth of ferrite thin films to spin-polarized tunnelling, *J. Phys. D Appl. Phys* **46**, 143001 (2013).

[2] Matthias Opel, Stephan Geprags, Edwin P. Menzel, Andrea Nielsen, Daniel Reisinger, Karl-Wilhelm Nielsen, Andreas Brandlmaier, Franz D. Czeschka, Matthias Althammer, Matthias Weiler, Sebastian T. B. Goennenwein, Jurgen Simon, Matthias Svete, Wentao Yu, Sven-Martin Huhne, Werner Mader, and Rudolf Gross, Novel multifunctional

- [16] X. Yu, C.-F. Huo, Y.-W. Li, J. Wang, and H. Jiao, Fe<sub>3</sub>O<sub>4</sub> surface electronic structures and stability from GGA+U, *Surf. Sci.* **606**, 872 (2012).
- [17] M. Fonin, Y. S. Dedkov, R. Pentcheva, U. Rüdiger, and G. Güntherodt, Magnetite: A search for the half-metallic state, *J. Phys. Condens. Matter* **19**, 315217 (2007).
- [18] J. G. Tobin, S. A. Morton, S. W. Yu, G. D. Waddill, I. K. Schuller, and S. A. Chambers, Spin resolved photoelectron spectroscopy of Fe<sub>3</sub>O<sub>4</sub>: The case against half-metallicity, *J. Phys. Condens. Matter* **19**, 315218 (2007).
- [19] Y. S. Dedkov, U. Rüdiger, and G. Güntherodt, Evidence for the half-metallic ferromagnetic state of Fe<sub>3</sub>O<sub>4</sub> by spin-resolved photoelectron spectroscopy, *Phys. Rev. B Condens. Matter* **65**, 064417 (2002).
- [20] B. B. Nelson-Cheeseman, F. J. Wong, R. V. Chopdekar, E. Arenholz, and Y. Suzuki, Room temperature magnetic barrier layers in magnetic tunnel junctions, *Phys. Rev. B Condens. Matter* **81**, 214421 (2010).
- [21] L. M. B. Alldredge, R. V. Chopdekar, B. B. Nelson-Cheeseman, and Y. Suzuki, Complex oxide-based magnetic tunnel junctions with nonmagnetic insulating barrier layers, *J. Appl. Phys.* **99**, 08K303 (2006).
- [22] L. M. B. Alldredge, R. V. Chopdekar, B. B. Nelson-Cheeseman, and Y. Suzuki, Spin-polarized conduction in oxide magnetic tunnel junctions with magnetic and non-magnetic insulating barrier layers, *Appl. Phys. Lett.* **89**, 182504 (2006).
- [23] J. M. Iwata-Harms, R. V. Chopdekar, F. J. Wong, B. B. Nelson-Cheeseman, C. A. Jenkins, E. Arenholz, and Y. Suzuki, Magnetotransport in La<sub>0.7</sub>Sr<sub>0.3</sub>MnO<sub>3</sub>/CuCr<sub>2</sub>O<sub>4</sub>/Fe<sub>3</sub>O<sub>4</sub> magnetic junctions, *Appl. Phys. Lett.* **106**, 012405 (2015).
- [24] G. Hu and Y. Suzuki, Negative Spin Polarization of Fe<sub>3</sub>O<sub>4</sub> in Magnetite/Manganite-Based Junctions, *Phys. Rev. Lett.* **89**, 276601 (2002).
- [25] G. Hu, R. Chopdekar, and Y. Suzuki, Observation of inverse magnetoresistance in epitaxial magnetite/manganite junctions, *J. Appl. Phys.* **93**, 7516 (2003).
- [26] H. Kaiju, T. Nagahama, S. Sasaki, T. Shimada, O. Kitakami, T. Misawa, M. Fujioka, J. Nishii, and G. Xiao, Inverse tunnel magnetocapacitance in Fe/Al-oxide/Fe<sub>3</sub>O<sub>4</sub>, *Sci. Rep.* **7**, 2682 (2017).
- [27] Y. J. Kim, Y. Gao, and S. A. Chambers, Selective growth and characterization of pure, epitaxial  $\alpha$ -Fe<sub>2</sub>O<sub>3</sub>(0001) and Fe<sub>3</sub>O<sub>4</sub>(001) films by plasma-assisted molecular beam epitaxy, *Surf. Sci.* **371**, 358 (1997).
- [28] See Supplemental Material at <http://link.aps.org-supplemental/10.1103/PhysRevApplied.15.034042> for additional data and explanations.
- [29] Y. Goto, T. Yanase, T. Shimada, M. Shirai, and T. Nagahama, Tunnel magnetoresistance effect in a magnetic tunnel junction with a B2-Fe<sub>3</sub>Sn electrode, *AIP Adv.* **9**, 085322 (2019).
- [30] F. Walz, The verwey transition - a topical review, *J. Phys. Condens. Matter* **14**, R285 (2002).
- [31] J. García and G. Subías, The verwey transition—a new perspective, *J. Phys. Condens. Matter* **16**, R145 (2004).
- [32] E. J. W. Verwey, Electronic conduction of magnetite (Fe<sub>3</sub>O<sub>4</sub>) and its transition point at low temperatures, *Nature* **144**, 327 (1939).
- [33] H. Yanagihara, M. Myoka, D. Isaka, T. Niizeki, K. Mibu, and E. Kita, Selective growth of Fe<sub>3</sub>O<sub>4</sub> and  $\gamma$ -Fe<sub>2</sub>O<sub>3</sub> films with reactive magnetron sputtering, *J. Phys. D Appl. Phys.* **46**, 175004 (2013).
- [34] Z. Huang, W. Liu, J. Yue, Q. Zhou, W. Zhang, Y. Lu, Y. Sui, Y. Zhai, Q. Chen, S. Dong, J. Wang, Y. Xu, and B. Wang, Enhancing the spin-orbit coupling in Fe<sub>3</sub>O<sub>4</sub> epitaxial thin films by interface engineering, *ACS Appl. Mater. Interfaces* **8**, 27353 (2016).
- [35] Yongxiong Lu, J. S. Claydon, E. Ahmad, Yongbing Xu, S. M. Thompson, K. Wilson, and G. van der Laan, XPS and XMCD study of Fe<sub>3</sub>O<sub>4</sub>/GaAs interface, *IEEE Trans. Magn.* **41**, 2808 (2005).
- [36] W. Q. Liu, M. Y. Song, N. J. Maltby, S. P. Li, J. G. Lin, M. G. Samant, S. S. P. Parkin, P. Bencok, P. Steadman, A. Dobrynin, Y. B. Xu, and R. Zhang, X-ray magnetic circular dichroism study of epitaxial magnetite ultrathin film on MgO(100), *J. Appl. Phys.* **117**, 17E121 (2015).
- [37] P. Morrall, F. Schedin, G. S. Case, M. F. Thomas, E. Dudzik, G. van der Laan, and G. Thornton, Stoichiometry of Fe<sub>3- $\delta$</sub> O<sub>4</sub> (111) ultrathin films on Pt(111), *Phys. Rev. B Condens. Matter* **67**, 214408 (2003).
- [38] X. H. Liu, A. D. Rata, C. F. Chang, A. C. Komarek, and L. H. Tjeng, Verwey transition in Fe<sub>3</sub>O<sub>4</sub> thin films: Influence of oxygen stoichiometry and substrate-induced microstructure, *Phys. Rev. B Condens. Matter* **90**, 125142 (2014).
- [39] J. P. Shepherd, J. W. Koenitzer, R. Aragón, J. Spalek, and J. M. Honig, Heat capacity and entropy of nonstoichiometric magnetite Fe<sub>3(1- $\delta$ )</sub>O<sub>4</sub>: The thermodynamic nature of the verwey transition, *Phys. Rev. B Condens. Matter* **43**, 8461 (1991).
- [40] F. Schedin, E. W. Hill, G. van der Laan, and G. Thornton, Magnetic properties of stoichiometric and nonstoichiometric ultrathin Fe<sub>3</sub>O<sub>4</sub>(111) films on Al<sub>2</sub>O<sub>3</sub>(0001), *J. Appl. Phys.* **96**, 1165 (2004).
- [41] A. R. Muxwworthy, Low-temperature susceptibility and hysteresis of magnetite, *Earth Planet. Sci. Lett.* **169**, 51 (1999).
- [42] X. H. Liu, W. Liu, and Z. D. Zhang, Evolution of magnetic properties in the vicinity of the verwey transition in Fe<sub>3</sub>O<sub>4</sub> thin films, *Phys. Rev. B Condens. Matter* **96**, 094405 (2017).
- [43] G. Kresse and J. Hafner, Ab initio molecular dynamics for liquid metals, *Phys. Rev. B Condens. Matter* **47**, 558 (1993).
- [44] G. Kresse and D. Joubert, From ultrasoft pseudopotentials to the projector augmented-wave method, *Phys. Rev. B Condens. Matter* **59**, 1758 (1999).
- [45] J. P. Perdew, K. Burke, and M. Ernzerhof, Generalized Gradient Approximation Made Simple, *Phys. Rev. Lett.* **77**, 3865 (1996).
- [46] J. Inoue, S. Honda, H. Itoh, K. Mibu, H. Yanagihara, and E. Kita, Effects of impurity states on exchange coupling in Fe/Fe<sub>3</sub>O<sub>4</sub> junctions, *Phys. Rev. B Condens. Matter* **85**, 184431 (2012).
- [47] S. L. Dudarev, G. A. Botton, S. Y. Savrasov, C. J. Humphreys, and A. P. Sutton, Electron-energy-loss spectra and the structural stability of nickel oxide: An LSDA+U study, *Phys. Rev. B Condens. Matter* **57**, 1505 (1998).